EES Batteries

Accepted Manuscript

This article can be cited before page numbers have been issued, to do this please use: G. Gammaitoni, G. Cha, R. R. Kolan, S. Christiansen, F. Fauth and M. Bianchini, *EES Batteries*, 2025, DOI: 10.1039/D5EB00188A.

View Article Online
DOI: 10.1039/D5EB00188A

Sodium-ion batteries (SIBs) are a novel technology that can complement Li-ion batteries (LIBs). SIBs would be strongly preferable in terms of abundance of raw materials, cost and sustainability, yet they suffer of lower energy density which ultimately hinders their widespread adoption. One of the causes of low energy density, specific and especially gravimetric, are the amorphous hard carbon (HC) anodes which are required since graphite, used in LIBs, does not store sodium ions. A possible way to increase their energy density is to prepare composites of HC with metallic elements that alloy with sodium. A limited amount of such alloying elements can allow to increase the capacity, without suffering of their main drawback, i.e. excessive volume expansion during electrochemical cycling. Here we report the reprodubile preparation of HC-Sn composites using an acqueous, scalable spray-dry process. After discussing the physicochemical properties of the composites and quantifying in detail the Sn content, we demonstrate the Sn electrochemical activity. The cycling performances obtained indicate higher specific and especially volumetric capacity, as well as excellent long term stability. The detailed analysis of our hard carbon-Sn composites can lead to further optimised materials which will contribute to the advancement of sustainable sodium-ion technologies.

Spray-dried Hard Carbon – Sn composites for energy-dense Na-ion batteries

Giovanni Gammaitoni[1,2], Gihoon Cha[3], Rajkumar Reddy Kolan[3], Silke Christiansen[3], François Fauth[4], Matteo Bianchini[1,2,*]

1 Faculty of Biology, Chemistry and Earth Sciences, University of Bayreuth, Universitätstraße 30, 95447 Bayreuth, Germany

2 Bavarian Center for Battery Technology (BayBatt), Weiherstraße 26, 95448 Bayreuth, Germany

3 Fraunhofer Institute for Ceramic Technologies and Systems IKTS, Äußere Nürnberger Straße 62, 91301 Forchheim, Germany

4 CELLS-ALBA Synchrotron, Cerdanyola del Vallès, 08290 Barcelona, Spain

* matteo.bianchini@uni-bayreuth.de

Abstract

Sustainability and availability of raw materials, besides the usual performance-related metrics, have become crucial aspects for the development of new battery technologies complementing the existing successful Li-ion. Sodium-ion batteries (SIBs) are at the forefront in this respect; however, the development of electrode materials meeting the expected performances is a challenge. Hard carbons (HC) are the most used anode material for SIBs, but the poor gravimetric and volumetric capacity have limited the development of energy-dense SIBs. High-density and high-capacity metals that can react with sodium through formation/alloying reactions represent a possible solution, but the huge volume expansion during electrochemical cycling limits their utilization. In this work we explore the synthesis and characterization of sustainable hard carbon-Sn composites as anode materials for Na-ion batteries, with the aim of increasing HC performance without suffering the side effects of Sn volume expansion. Starting from conventional HC synthesis we propose a water-based continuous-flow spray drying process to prepare our composites, resulting in an increase in HC´s gravimetric and volumetric performances, including better long cycling stability. By using a set of analytical tools, we reveal the different physicochemical properties of our composites as a function of the starting cellulose precursors. The amount of Sn in the composites has been carefully evaluated through several techniques and lies at ≈15 or ≈25 wt% depending on the Sn content used for the synthesis. The activation of Sn during electrochemical discharge has been confirmed by operando synchrotron XRD, and the results show the appearance of sodiated Sn phases forming in kinetically driven reactions that do not fully adhere to the expected thermodynamic phase diagram. The electrochemical testing of our materials, carried out using conventional carbonate-based electrolytes, demonstrates excellent performances, with one composite demonstrating 301 mAh/g of capacity after 100 cycles (94% retention). Noteworthy is that the volumetric energy density is also significantly improved. Finally, by synthesizing several HC-Sn composites using alternative methods we demonstrate how spray-drying leads to superior performances, especially in terms of capacity retention. Our work establishes the feasibility of spray drying as scalable and sustainable synthesis route to prepare high-performance negative electrode composites for Na-ion batteries.

Introduction

View Article Online
DOI: 10.1039/D5EB00188A

Sodium-ion Batteries (SIBs) are widely investigated as an energy storage system able to offer alternative solutions to the increasing energy storage demand [1]. They were developed in the past century in parallel with Lithium-ion Batteries (LIBs)[2] [3] [4], but the latter had a huge success and faster commercialization thanks to the lower molecular mass of Li and the higher operating voltage of the cell, resulting in higher gravimetric and volumetric energy density (Wh/kg and Wh/L) [5]. However, the critical situation of lithium resources and its fluctuating price has pushed scientists to find alternatives for LIBs. The challenge lies in the fact that SIBs can't provide the same performances of the best LIBs based on graphite and NCM electrodes; yet recently it has been shown that a NVP/HC sodium-ion battery ($Na_3V_2(PO_4)_3$/Hard Carbon) can achieve a performance close to the $LiFePO_4$/graphite (LFP/Gr) lithium-ion battery [6]. NVPF/HC cells ($Na_3V_2(PO_4)_2F_3$/Hard Carbon) have been commercialized by the French startup Tiamat [7], while several Chinese companies such as CATL offer layered oxide-based SIBs. The challenge is now to bridge the gap to LFP-based LIBs, to mitigate the expected huge demand of lithium in the next years[8]. For both cells' technology, a determinant limiting factor is the low density of the carbon anode, that reduces the overall volumetric energy density (Wh/L). In LIBs, graphite can reach a density of 2.3 g/cm^3, while Hard Carbons in SIBs typically have a lower density close to 1.5 g/cm^3 [9]. Even though the specific gravimetric capacity of these materials is similar (372 vs ≈ 300 mAh/g), the lower density of HC contributes to the lower volumetric performances of SIBs. In the last years, scientists have tried to improve the volumetric energy density of LIBs and SIBs by using different carbon-based anodes, synthesized via innovative and cutting-edge methods and potentially achieving specific capacities well beyond the mark of 300 mAh/g [10] [11]. However, these syntheses are often hard to scale-up beyond the laboratory scale.

A widely recognized solution to increase the performance of the anode is replacing the carbon-based materials with elements that have the ability to alloy with Na, e.g. Sn, Ge, Sb, P, Pb [12] [13] [14] [15] [16]. These exhibit high density and hence high specific gravimetric capacity (up to 10^3 mAh/g) when the high sodium content phases are formed during electrochemical discharge[15] [17]. A special attention has been given to Sn[18] [19], since it shows a high theoretical gravimetric capacity (847 mAh/g), a high density (7.31 g/cm^3), and it is relatively abundant and non toxic. However, as is well-known in the case of Si for LIBs, these materials suffer from a huge volume expansion during the sodiation process [20], leading to a pulverization of the electrode and a short cell lifetime. Moreover, it's important to note that most of the synthesis methods reported in literature involve special steps that are often applicable only to a laboratory scale synthesis, e.g. chemical vapour deposition (CVD), ball milling, using of templates and solvothermal treatments[16]. To mitigate the issue of excessive volume expansion, the scientific community focussed on preparing blends or composites of carbon and alloying elements. The first attempts were done for LIBs[21] [22] [23] [24] [25], and later for SIBs[26] [27] [28], but again many proposed synthesis are not scalable. Nonetheless in many commercialized LIBs today a blend of graphite and silicon constitutes the anode, but only ≈10% of silicon is included in the composite to avoid excessive volumetric expansion and prevent electrode pulverization.

A promising scalable synthesis method for the production of composites is spray drying, which has been demonstrated in the preparation of anodes for LIBs and SIBs [29] [30]. A recent comprehensive study on alloying elements for SIBs has proposed to not overcome the volume expansion that is found in the graphite/Si blend, limiting the alloying weight % in the hypothetic HC/alloying-element blend in SIBs anode [31]. It has been also demonstrated that ether-based electrolytes can mitigate the pulverization process by stabilizing the solid electrolyte interphase (SEI) that grows homogeneously on the surface of the anode and doesn't become too thick (as compared to its evolution in commercial carbonates based electrolytes)[32] [33]. However, ether-based electrolytes are typically unstable at high voltages, and deeper

View Article Online
DOI: 10.1039/D5EB00188A

research is still required in the optics of combining optimized anodes and high voltage cathodes to assemble full cells [34]. Therefore, the most used electrolytes remain carbonate-based ones that perform well at high voltages and represent a simple drop-in solution from the LIB technology.

For these reasons, in this work we explore ways to increase the performance of HC via the incorporation of Sn using spray-drying as a green and scalable method. Spray drying allows a continuous synthesis with a product yield that only depends on the reactants amount, with no facility restriction. We synthesized HC-Sn composites and compared their performances and characteristics to the pristine HC. Morphology and microstructures are studied to understand the modifications induced by the spray drying synthesis, and the cell performances are tested in electrochemical cycling tests. Using a carbonate-based electrolyte, we demonstrate the improvement of the HC-Sn composite performances, also comparing spray-drying to other methods. Furthermore, we clarify the functioning mechanism of the composite.

Experimental section

Materials synthesis

Hard carbons (HCs) were synthesized by a two-step heat treatment: we used two different cellulose precursors from Sigma-Aldrich, one is colloidal (microcrystalline) here named CC, and the other one is in fibers (microcrystalline powder 20 μm), here named FC. They are initially treated in a Linn furnace under synthetic air atmosphere for 12 hours at 300 °C, and then the final carbonization takes place in a Carbolite furnace at 1400 °C for 1 hour. The heating rate is 5 °C/min and then the samples are naturally cooled down. Then, HC and Sn nanoparticles (Tin Nanopowder 99.9%, 60-80 nm, US Research Nanomaterials) are used as precursors for the synthesis of HC-Sn composites (HC:Sn = 2.34:1). We used a Buchi spray dryer (Mini spray dryer B-290), and we set the inner temperature to 180 °C, the pumping rate to 30 % and the aspirator to 100 %. The synthesis happens in air. We labelled the composites as CC-Sn and FC-Sn, named after the HC used for the synthesis. Two more composites were prepared targeting the HC:Sn ratio equal to 1, and they are labelled CC-Sn_50 and FC-Sn_50. The effect of the spray-dry process on HCs has also been determined by repeating the spray drying synthesis without Sn nanoparticles. Two reference pairs of samples have been synthesized to compare the performance of spray dried samples; the first synthesis involves hand mixing of HCs and Sn nanoparticles in a mortar for 10 minutes, while the second synthesis has been done in a planetary ball milling (Fritsch, Pulverisette 7) for 6 hours at 600 rpm (balls:AM wt ratio equal to 20).

Material characterization methods

Powder x-ray diffraction (XRD) patterns were collected at the MSPD beamline (ALBA synchrotron) with a position sensitive detector MYTHEN2 (wavelength λ = 0.62020 Å) and in laboratory using a Stoe StadiP diffractometer with a Mythen2K detector in Debye–Scherrer geometry equipped with a monochromatic Mo-$K\alpha_1$ radiation (wavelength λ = 0.70932 Å). The acquisition was performed on powder packed in a 0.5 mm diameter borosilicate glass capillary. Then we performed the Rietveld refinement using the FullProf Suite. The operando synchrotron x-ray powder diffraction (SXRPD) has been done at the same beamline on coin cells equipped with a quartz window, in half cell configuration. The experiment has been done at 50 °C in a coin cell chamber where thermalization is guaranteed by the continuous circulation of a silicon oil, as carefully described in the literature [35]. Patterns have been taken every 10 minutes with an effective integration time of 20 seconds.

View Article Online
DOI: 10.1039/D5EB00188A

TGA experiments were performed on a simultaneous thermal analyser (STA) model STA 449 F5 "Jupiter" (Netzsch) connected to a mass spectrometer for evolved gas analysis (QMS Aëolos Quadro model 8QMS403Q), with a protocol that involves heating to 600 °C with a rate of 5 °C/min and hold for 3 hours, followed by a natural cooling. CO_2 evolution was monitored by following the channel m/z = 44.

For Raman spectroscopy the samples were pelletized under a pressure of 0.5 MPa. The measurements were carried out with a WITEC ALPHA 300 RA+ instrument at the Keylab "Synthesis and Molecular Characterization" of the University of Bayreuth, using a wavelength of λ = 532 nm and a power of ca 7.0 mW. The spectra were taken with a number of accumulations of 50 and integration time of 0.5 s.

Gas pycnometer (Anton Paar Ultrapyc 5000 micro) was used for the determination of the density of the samples at the BayBatt Keylab of the University of Bayreuth. The volume of the material was determined by 15 runs with He gas.

SEM and ex situ SEM-EDX was performed with a ThermoFischer Scientific Phenom ProX microscope on powder samples, with a magnification of 5000x and 1000x, an acceleration voltage of 15 kV and BSD and SED detectors. Before conducting the ex situ measurements, the samples were carefully washed with DMC and dried under vacuum. For electrode samples a LEO-1530 electron microscope was used at the Keylab "Electron and Optical Microscopy" of the University of Bayreuth, with a magnification of 500x, an acceleration voltage of 3 kV and ESB detector.

SAXS patterns were collected at the Keylab "Mesoscale Characterization: Scattering Techniques" of the University of Bayreuth in a q range of 0.001-1 $Å^{-1}$. The acquisition was performed on powder packed in a 0.3 mm diameter borosilicate glass capillary. The measurements were performed in transmission geometry using a Double Ganesha AIR system (SAXSLAB) with a copper anode for x-rays source (wavelength λ = 1.5406 Å) and a PILATUS 300 K, Dectris detector. For the data treatment, the blank of the empty capillary was subtracted. The data were fitted with the software SASfit.

The BET surface area was determined from N_2 absorption experiments on a Quantachrome Autosorb 1 at the Chair of Inorganic Colloids for Electrochemical Energy storage of the University of Bayreuth. All samples were carefully outgassed at 150 °C under ultra-high vacuum overnight prior to measurements and liquid N_2 was used to cool down the system for the measurement. Quenched solid density functional theory (QSDFT) method has been used to determine the pore size distributions and the pore widths[36]. The employed model takes into account the adsorption branch of N_2 at 77 K on carbon considering slit/cylindrical shape of pores.

The porosity and volumetric composition of the electrode components, including hard carbon, Sn, and binder plus conductive carbon were analyzed using x-ray Microscopy (XRM). The imaging experiments were performed with a Zeiss Xradia 620 Versa (Carl Zeiss x-ray Microscopy Inc., Pleasanton, CA, USA). This system employs a cone-beam x-ray source and utilizes geometric and optical magnification to achieve high spatial resolution. The x-ray source generates a tunable polychromatic beam with a tungsten target, where the acceleration voltage can be adjusted to optimize imaging conditions. The XRM scans were conducted using a 20× objective lens to achieve high spatial resolution, with the source operated at a voltage of 50 kV and a power of 4.5 W. The imaging conditions included an air filter, an exposure per frame of 0.7 s, and 44 frames in total, enabling high-contrast volumetric data acquisition. Electrode samples with a diameter of 13 mm were carefully mounted onto a sharpened mechanical pencil lead and fixed into a custom-designed homemade holder to ensure stability

View Article Online
DOI: 10.1039/D5EB00188A

during imaging while minimizing motion artifacts. The acquired XRM projection images were reconstructed using proprietary software (Zeiss XMReconstructor, Carl Zeiss x-ray Microscopy Inc., Pleasanton, CA, USA) with a filtered back-projection algorithm, and post-processing and visualization were conducted using XamFlow (Lucid Concepts AG, Zürich, Switzerland). The volumetric images obtained were utilized to determine the porosity and volumetric fractions of the electrode components by applying simple thresholding techniques for the identification and segmentation of key materials. The volume occupied by each component was calculated within a cubic volume of 0.00018 cm³ (120 µm × 1000 µm × 1500 µm) using the XamFlow workflow tool.

Electrochemical measurements

Anodes were prepared by wet casting on Al foil. For slurry preparation we used different strategies in function of the active material used. For the HCs, we mixed the active materials with the binder in the ratio of 95:5, while for the HC-Sn composites we also added the conductive carbon (Super P, Alfa Aesar, 99%), resulting in the ratio of 70:10:20. For the design of HC electrodes, there are different studies in literature where several combinations of binders are tested [37] [38]. In this work we tested PVDF and a mixture of CMC:SBR with our materials and we found that the optimal binder differs in function of the morphology of the HC. Initially, two 7.5 % solutions of binder dissolved in the solvent were prepared: we used PVDF in NMP (*N*-Methyl-2-pyrrolidone, Sigma-Aldrich, 99.5%) and a blend of CMC:SBR (1:1) (CMC: carboxymethylcellulose, Dupont; SBR:styrene-butadiene rubber, MTI Corp.) in water (VWR chemicals water). We mixed the binder with the active materials and the conductive carbon in a mixer (THINKY ARE-250) and casted the slurry on Al foil. The slurries were dried overnight at a temperature of 100 °C for NMP based ones, and 60 °C for the water-based ones. Then the electrodes were cut in 13 mm diameter disks with a steel puncher. The loading of HC and HC-Sn materials is 3-4 mg/cm^2. For the electrochemical testing, we prepared 2032-type coin cells in half cell configuration in an argon-filled glove box (200 B, MBraun, Germany; H2O < 0.1 ppm, O2 < 0.1 ppm), with two layers of porous glass separators (Whatman GF/A) and Na metal as counter electrode (prepared from dry stick, Thermo Scientific, 250 µm thickness). We used 90 µL of electrolyte, and we tested 1M $NaPF_6$ in EC:PC (1:1) and in diglyme. Capacity retention tests were conducted at C/10 (1 C = 250 mA/g) and at the end of the discharge a CV step is added until the current has reached the value of C/30. For the rate capability tests, we subsequently increased the C-rate from C/10 to 2C and increasing the cut off limit of the current in the CV step from C/30 to C/3. The cut off voltage for all the tests is 0.002-2 V vs. Na^+/Na.

Results and discussion

Structure of carbons and composites

Hard Carbon (HC) and HC-Sn composites have been synthesized as described in the methods section. SEM images (Figure 1) show the morphology of the samples made with different starting cellulose precursors. Clear differences between them can be noticed: the HC obtained from colloidal cellulose named CC reveals a rough surface and a potato-like shape, while the HC obtained from fiber cellulose named FC is composed of elongated and smoother particles. More SEM images are shown in figure S1 with lower magnification as significant statistical sampling. The Sn-containing composites are named CC-Sn and FC-Sn. During the spray drying process, Sn nanoparticles find space in the cavities of CC, and they can be located on its surface. In the case of FC, Sn nanoparticles seem to have less surface roughness and appear to lay on the surface. Despite some agglomeration (visible in Figure S1), Sn appears to retain its nanometric size and it is better accommodated on the surface of CC rather than of FC.

View Article Online
DOI: 10.1039/D5EB00188A

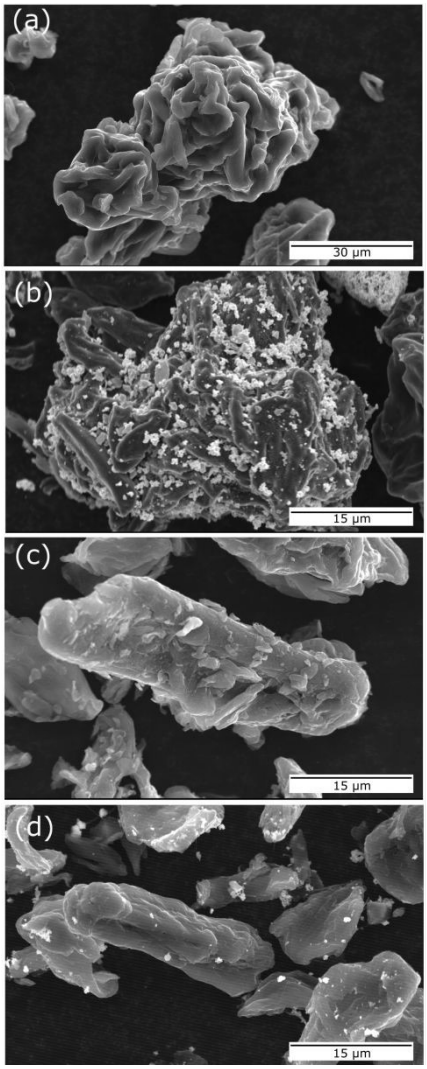

Figure 1: *SEM images of (a) hard carbon from colloidal cellulose (CC), (b) composite CC-Sn, (c) hard carbon from fiber cellulose (FC), (d) composite FC-Sn.*

Several methods have been used to highlight the differences between HCs and between HCs and the respective HC-Sn composites, as summarized in Figure 2. Firstly, the surface area of the samples has been measured via BET method. Figure S2 displays the curves of the volume of adsorbed (desorbed) N_2 in function of the relative pressure. The effect of the spray-dry process on the HC's surface area (without Sn addition) has been determined as well. Figure 2b and Table S1 report the measured BET surface area of all the samples. A quick comparison of the HC reveals that CC exhibits a lower surface area than FC (due to CC´s bigger particles size, see figure S1), highlighting the morphological differences of these two samples. In our study, morphology of HC plays a big role, since usually in literature different values of surface area are observed for samples treated at different temperatures (usually between 1000 and 1600 °C), while our HCs have been treated at the same carbonisation temperature of 1400 °C [39] [40]. So the difference in the precursors makes the surface area of FC bigger than CC by one order of magnitude. As already well known in literature, a low surface area is beneficial for sodium storage, as it determines a higher initial coulombic efficiency since less Na is irreversibly trapped in the SEI[41] [42]. For this reason, we expect a different behaviour of the HCs during electrochemical cycling. Nevertheless the two hard carbons exhibit different particle size, and we also expect this parameter to have a strong effect on the electrochemistry. The spray drying process alone (without Sn) has a huge impact on HCs,

View Article Online
DOI: 10.1039/D5EB00188A

since they both experience an increase in the surface area probably due to formation of surface defects during the process (Table S1). After spray-drying of HCs with Sn nanoparticles, the composites show a further increase in surface area, due to the presence of nanoparticles on the surface of HCs that make the N_2 adsorption more favourable. Moreover, Figure S3 represents the pore size distribution of the samples and table S2 their pore width, as obtained via DFT methods[36]. Note that being determined by BET, these porosities refer to the accessible (open) porosity on the surface of the particles, as opposed to the internal (closed) porosity existing in HCs, that we will discuss later. One can observe that the pore width of the two HCs does not appear to be significantly different. On the other hand, both composites show bigger pore width compared to the pristine HC, as evidence of Sn surface modification. In previous studies the effect of temperature on HC pore width has been taken into account, revealing that higher synthesis temperature is translated in bigger and less abundant pores compared to the ones observed at lower synthesis temperatures[39]. In our study the discriminant among our HCs is represented by the different cellulose precursors only, therefore a strong and clear correlation is not present. CC shows a variegated outer porosity, since micropores and mesopores are present in comparable amount with multiples pore widths. The most abundant micropores have a width of ≈ 7 Å while the most abundant mesopores have a width of ≈ 55 Å. FC has more and smaller micropores than CC with a width of ≈6 Å, and a little amount of mesopores with a width of ≈ 60 Å. After the spray treatment without Sn, the micropores on sample CC become predominant and more abundant than in CC, while in FC a multiplicity of micropores is formed with a width that covers the range between 5 and 10 Å. The spray drying step is crucial in the morphological modification of the HC. After the Sn mixing, the two composites exhibit similar features, with a comparable abundance of micropores.

Our aim is to increase the volumetric energy density of sodium anode materials, so we measured the density of our materials by pycnometry (figure 2c). The expected trend can be observed, where the composites show higher density compared to the relative pristine HC. However, assuming that the density of the composites is given by the sum of the densities of HC and Sn multiplied by the nominal weight % fraction, we only get 64% and 76% of the expected density for CC-Sn and FC-Sn respectively. When repeating the calculation with the actual Sn wt% (determined in the next section), a closer value of 80% and 96% is obtained. The reason behind the persisting underestimation of density can be reconducted to the surface area of our materials. Since the pycnometer measures the difference in pressure among the analysed sample and a blank reference when a gas flows in the instrument to determine the volume of interest, if the probing gas is partly trapped in the material we must expect an underestimate of the density. Thus, considering that for the volume determination the gas can only access open pores and that some of it may remain trapped in the surface defects in high surface area samples, we can state that the obtained values from pycnometry represent a lower bound for the samples' density.

Beyond the surface area of the samples, HCs are mainly known for their internal structure[43] [44]. The inner structure of the best performing HC is abundant in micropores, and in most of the cases they are closed pores[45] [46] [47]. These features allow the HC to avoid parasitic reactions with the electrolyte which cannot access the closed pores and contribute to the formation of a small SEI. Only Na can access the closed pores during the electrochemical discharge step, leading to the huge plateau usually observed at ≈10 mV vs Na^+/Na, often attributed to Na plating in such closed pores. To probe these pores, we used small angle x-ray scattering (SAXS), as reported in Figure 2d. In the SAXS patterns, a shift towards higher intensity is observed at low q values in the composites patterns, and this phenomenon could

View Article Online
DOI: 10.1039/D5EB00188A

be attributed to the effect of the difference of electron density (ρ) of Sn and C. In SAXS theory, the intensity goes as

$$I\,(q) \propto \Delta\rho^2 \tag{1}$$

and in HC samples the only contribution comes from C and air present in the closed pores and surrounding the HC. In the composites, we add another contribution, coming from Sn particles and air. Since

$$\rho_{Sn} - \rho_{air} > \rho_C - \rho_{air} \tag{2}$$

we justify the observed intensity shift. In the high q region, we observe the shoulder describing the closed micropores, and it is present in all our materials with a good overlap. We can state that no significant difference in the micropores has been inducted by Sn incorporation, as one could expect.

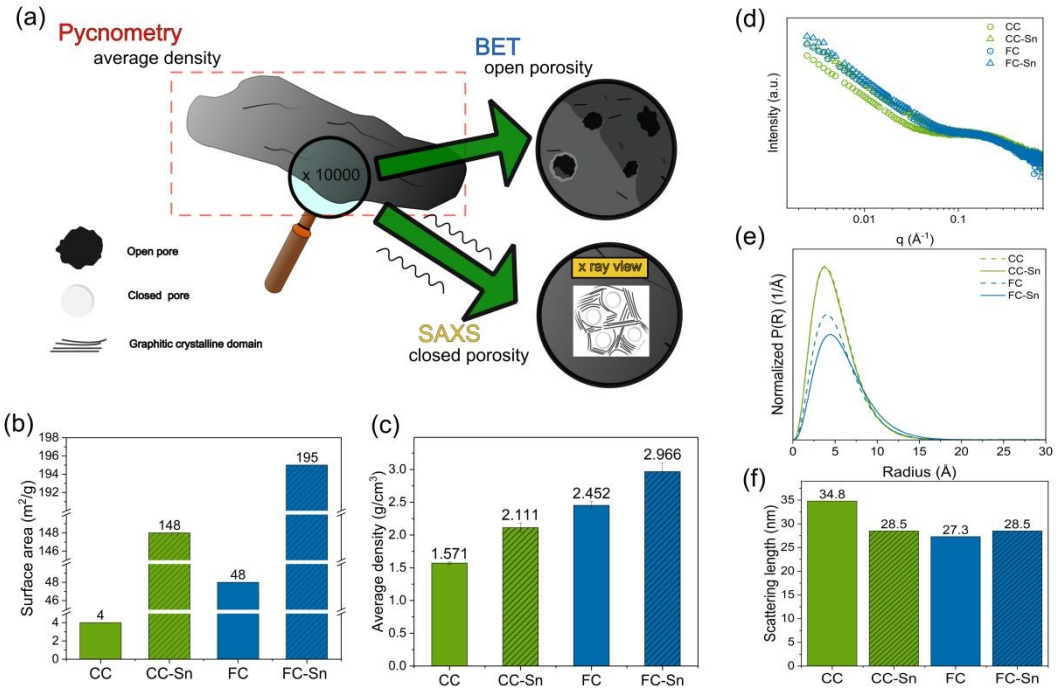

Figure 2: (a) *Qualitative sketch of the structure of HCs. Pycnometry gives the average density of the entire particle, while a proper magnification on the surface (SEM, BET) shows open pores (meso/micropores). An x-ray view (SAXS) shows bulk closed micropores encapsulated in defective graphitic domains. (b) Surface area values of the samples obtained via BET. (c) Density values from He pycnometry and (d) SAXS patterns of HCs and composites. Tin incorporation results in the increasing of the HCs density and in the shift towards higher intensity in SAXS patterns. (e) Pore size distribution and (f) scattering length of HCs and composites.*

Based on previous works on operando SAXS on HC[48], we fitted our data using different contributions:

$$I\,(q) = I_{particles}\,(q) + I_{pores}\,(q) + I_{Sn}\,(q) + I_{background} \tag{3}$$

View Article Online
DOI: 10.1039/D5EB00188A

where the particles term is a power law (Porod model) and the background term is a constant. For the pores contribution, spherical particle model and Schulz-Zimm distributions are used, while for Sn term we used the LogNorm distribution. SAXS fits are shown in figure S4, and the effect of Sn contribution is shown in figure S5, where we subtracted the contribution of the particles to show that the contribution of the pores alone can't fit properly the experimental data. The pore size distribution is shown in figure 2e, and for all the materials the average pore radius falls in a range that is in good agreement with the value of HC synthesized at 1400 °C in literature[39] [48]. However, we can find some differences in these values among our materials, since the samples CC and CC-Sn show an average pore radius of 3.93 Å, while FC and FC-Sn show a value of 4.25 and 4.55 Å respectively, and less pores. Based on recent studies on sodiation of HC, it has been found that Na^+ experiences a transformation to quasi-metallic behaviour and agglomerates in clusters in closed pores[49] [50] [51]. Bigger closed pores can store more quasi-metallic Na ions, therefore large size and high abundance are the key parameter for high Na^+ storage in HC materials [52]. These differences are supposed to give different performances in electrochemical tests, as we will verify in the following.

We also extrapolate the values of the characteristic scattering length of the physical object (figure 2f), by fitting the region at low q with the power law only, and recording the q value when the fit shows an error of 10 % (figure S6), and applying the formula:

$$d = \frac{2\pi}{q} \quad (4)$$

The power law describes the scattering behaviour of a sharp surface of a material in a medium[53] [54]. A deviation from this regime indicates that the interface is not well defined anymore, but it becomes more diffused since the difference in electronic density of the two scattering media gets smaller. In the SAXS pattern this is translated in a more gradual transition with the increase of q, since the intensity does not decay as fast as in the low q region anymore. The structure of HC is complex and rich of defects, therefore it is tough to give an absolute interpretation of this physical object. From the reported HC structure models[8], it can be interpreted as the size of aggregated primary particles clusters on top of secondary particles that determine the breaking in the evenness of the surface. This makes the scattering length an indicator of the roughness of the material's surface, since for an ideal smooth particle we expect the power law to describe a longer range of q compared to an irregular surface. A comparison among CC and FC shows that the power law has a bigger range of validity for FC than CC since it shows a higher q limit value, confirming that FC particles have a more regular shape and their surface is more even and shows less defects than CC. In the composites, CC-Sn experiences a decrease in scattering length compared to CC, indicating that Sn is located in the roughness of CC and makes its surface more even, while FC-Sn shows a slight increase in the scattering length, signing that Sn increases the roughness of FC surface. This result is in agreement with SEM pictures of the materials, where the Sn distribution on the HCs is visible. A qualitative model of HCs is shown in figure 2a, representing the open pores analysed via BET and the closed pores determined by SAXS.

In order to characterize the carbon matrix, we also performed Raman spectroscopy. The spectra of all the materials are shown in figures S7 and S8. In the spectrum of carbonaceous material, we can find the presence of the G band (ca 1600 cm^{-1}) relative to the in plane stretching of sp^2 carbon atoms with E_{2g} symmetry, and the D band (1350 cm^{-1}) relative to the breathing of carbon atoms with A_{1g} symmetry[55] [56] [57]. The D band is usually related to defectiveness degree of the carbon material, and it is generated by the presence of carbon rings in the structure[55]. The ratio between the intensity of D band over G band is a useful

View Article Online
DOI: 10.1039/D5EB00188A

value to compare different carbonaceous materials, in order to evaluate the defectiveness degree of the structures[58]. The spectra of the two hard carbons are reported in figure S7. We adopted the Sadezky model to deconvolute the spectra, so we find the G and D band[59]. In this model the D band can be deconvoluted in multiple contributions, so we have the peaks of crystalline graphite microdomains (D1) disposed in disordered domains (D3, D4) and some general amorphous carbon vibrational contribution[60] [61] [62]. The parameters used for fitting are summarized in the SI (table S3). Here we report the first and second order of carbon, where the overtone bands (2D, 2D') and the lattice fundamental vibration modes (D+G) can be found[63]. Sn presence in the composites is revealed by the peaks at low Raman shift values. Raman spectrum of Sn nanoparticles has been taken as reference (figure S8f). In figure S8e we show the I_D/I_G values of our materials. The two HC show a similar value of ordering, so their morphology does not have a significant impact on the defectiveness that can be probed with Raman spectroscopy. However, in the composites we can appreciate a small change in this value. This suggests that the spray drying process induces or increases a mode in the D band, resulting in an increasing of defectiveness degree of the material, perhaps near the surface.

In summary, the results of the characterization of the HC and HC-Sn materials revealed that the mesostructure (surface area, scattering length and defectiveness) is strongly dependent on the morphology of HC, and it is affected by Sn incorporation via spray dry process. Comparing the HC samples, we find that CC shows a surface area one order of magnitude lower than FC, probably due to its bigger particles, and higher roughness as confirmed by SEM, BET and SAXS measurements. On the other hand, FC shows higher density and bigger closed pore size compared to CC. With both carbons, when Sn is incorporated, we observe an increase in surface area and in I_D/I_G, sign that Sn nanoparticles influence the active sites on the surfaces available for gas adsorption and induce the activation or enhancement of defective modes detected by Raman. On the other hand, Sn incorporation results in a decrease of roughness in CC, sign that the nanoparticles find room in hard carbon cavities, while it results in increase of roughness in FC, where no cavities are present, as revealed by SAXS and SEM. The microstructure (inner pores abundance and size) is instead not modified by the Sn incorporation, which is indeed rather affected by other parameter such as the synthesis temperature [40] [63].

Determination of Sn content

A potential drawback of spray drying is the unknown Sn loss during the process. Even though we prepared a Sn nanoparticles suspension for spray drying targeting 30% Sn content, it must be verified what amount is effectively incorporated. We then propose different methods to estimate the Sn amount in our materials by using scattering, thermal analysis, imaging and electrochemistry.

XRD is a valid tool to estimate the amorphous content of a material, by collecting a pattern of a blend of the sample with a known amount of a crystalline standard[64]. Here, we prepared one sample of our composites and Si as reference in ratio 10:1, packing a capillary to conduct the measurement. In table 2 we report the results of the amorphous phase estimation in the composites. In figures S9 and S10 the patterns of CC-Sn and FC-Sn are reported with the respective Rietveld refinement. By this method we find an amount of crystalline phase that is around 18.4 % for CC-Sn and 11.4 % for FC-Sn. We also tried to employ LaB_6 as reference material (table S4), but we obtained an estimated crystalline phase content around 5 % for CC-Sn and 5.5 % for FC-Sn. These low values are due to the huge difference in density between our materials and LaB_6 that does not guarantee the formation of a homogeneous

View Article Online
DOI: 10.1039/D5EB00188A

blend of sample-reference, so the measurement is strongly affected by sample preparation issues. Therefore we deem only the measurements performed with Si trustworthy.

Material	reference	λ (Å)	AM : reference	Amorphous content (%)	R_{Bragg} reference (%)	R_{Bragg} Sn (%)
CC-Sn	Si	0.70932	10 : 1	81.63 ± 1.69	6.99	6.94
FC-Sn	Si	0.70932	10 : 1	88.64 ± 1.05	6.56	4.66

Table 1: *data of XRD measurements and refinements with Si to quantify the amorphous phase in the composites.*

We also find that during the synthesis in water, some Sn undergoes oxidation resulting in poorly crystalline SnO and SnO_2, which can be noticed by the broad peaks shown in the diffraction patterns of Figure S9 and S10. This may also partially explain the low density values obtained by pycnometry for the composites, since we confirmed that some Sn oxidized in a less dense crystal structure than Sn. Due to the uncertainty introduced by these side phases, other methods to determine the Sn content were also investigated.

A technique that does not require assumptions on the crystal structure of the materials is thermogravimetric analysis (TGA), and it has already been used in literature to determine the Sn amount in Sn composites used as anodes for lithium-ion batteries[65]. In figure 3a we report the mass loss as function of time during the heating process up to 600 °C in air. Figure S11 shows the TGA experiment of Sn nanoparticles alone. At the end, the residual mass (Δm_{Sn}) recorded for Sn is 117.05 ± 0.28 %. This value lies between the ideal values obtained for the formation of SnO (113.48 %) and SnO_2 (126.95 %), hence the final chemical formula of the compound we obtained after Sn heating is SnO_x with 1<x<2. Knowing the residual masses of HC (Δm_{HC}) and composites ($\Delta m_{HC\text{-}Sn}$) and assuming that $\Delta m_{HC\text{-}Sn}$ is composed by the sum of Δm_{HC} and Δm_{Sn} we can use the following equation to determine the Sn amount in our materials:

$$Sn\ wt\ \% = \frac{\Delta m_{HC-Sn} - \Delta m_{HC}}{\Delta m_{Sn}} * 100 \quad (5)$$

By this method the amount of Sn in CC-Sn is found to be 18.42 ± 1.19 %, and in FC-Sn 13.31 ± 1.90 %. This values still confirm that some Sn is lost during spray drying, and we believe they are trustworthy as they don't depend on any feature of the samples. Moreover, Figure 3a also exhibits a mass spectrometer analysis (TGA-MS), where we followed the evolution of CO_2 during the heating process (channel m/z = 44) confirming that all the mass loss comes from oxidation of carbon. A direct proof of the effect of Sn in HC materials is definitely the increase of gravimetric capacity (mAh/g). As said before, in sodium ion batteries Sn shows its theoretical capacity and good performances in terms of capacity retention and electrode stability in ether-based electrolytes. Although we decided to focus on conventional carbonate-based electrolytes for this study, the usage of ethers can help us reveal the Sn content in our composites. In figure S12 the electrochemical performance of CC-Sn and FC-Sn with 1M $NaPF_6$ in dyglime is shown. Assuming that the total capacity of the composites is given by the HC and Sn capacities multiplied by their weight %, we obtain

$$Sn\ wt\ \% = \frac{Q_{HC-Sn} - Q_{HC}}{Q_{Sn} - Q_{HC}} * 100 \quad (6)$$

where $Q_{HC\text{-}Sn}$ is the experimental capacity of the composite, Q_{HC} is the experimental capacity of the HC and Q_{Sn} is the theoretical capacity of Sn (847 mAh/g). From this equation we obtain

View Article Online
DOI: 10.1039/D5EB00188A

a Sn amount for CC-Sn of 20.87 ± 0.18 %, and 13.65 ± 0.17 % for FC-Sn (based on the capacity of the 10th cycle). These values are in very good accordance with TGA results.

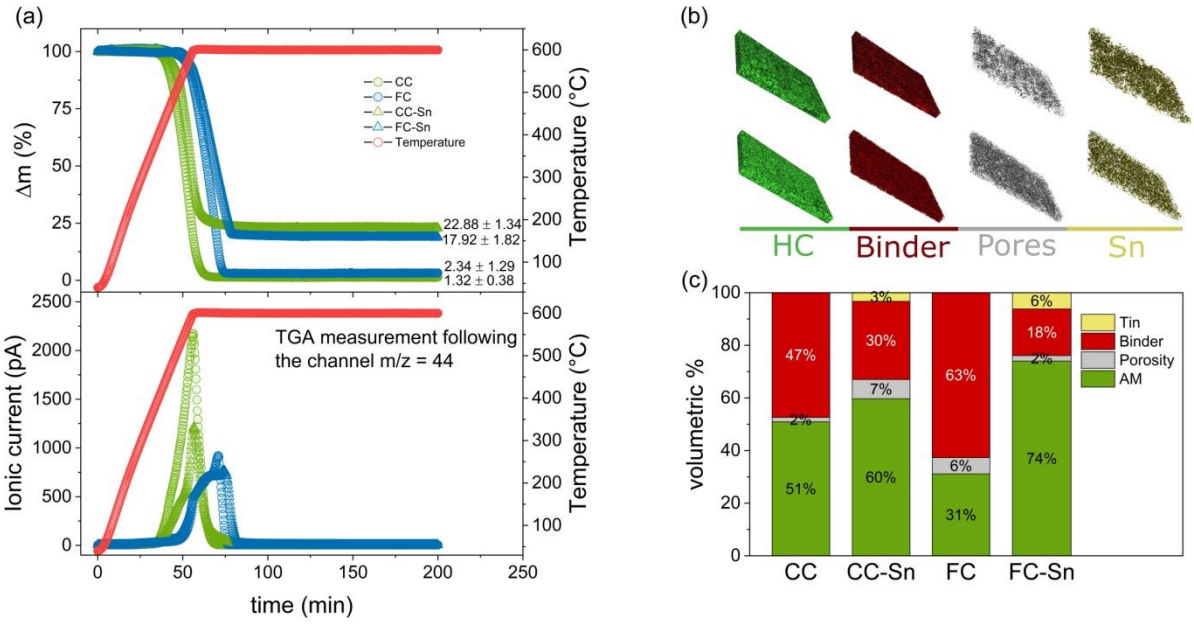

Figure 3: *(a) Residual mass in the HCs and composites after TGA-MS in air and relative ionic current given by CO_2 evolution. (b) 3D XRM reconstructions of the section of composites electrodes (CC-Sn on top and FC-Sn on the bottom). (c) Volumetric % of electrodes components.*

Finally, we employed x-ray tomographic imaging to further confirm the composites' structure and Sn distribution. Here, a known volume of the samples casted on aluminium (electrodes) has been cut and measured with x-ray microtomography (XRM). Starting from the known percentage of the components of the electrodes, it is possible to calculate the percentage of the active material, the binder, and the pores. The active material can moreover be distinguished among HC and Sn, so then a volumetric percentage of the components is given. In figure 3b we report a 3D reconstruction of the composite electrodes and in figure 3c the results of the data treatment to define the volumetric percentage of each component in the electrodes. The 3D reconstruction of the HC electrodes can be found in figure S13. The weight percentage (wt%) of each component was calculated based on the volumetric ratios extracted from the XRM data, with two key considerations: porosity was excluded from the weight percentage calculations due to the lack of density information, and the density of the binder plus conductive component was assumed to be 1.5 g/cm³. For the HC-Sn composites the density values obtained by pycnometry were used. These assumptions ensured consistency in the estimation of electrode composition.

We used the equation

$$w_i = \frac{V_i \cdot \rho_i}{\sum (V_i \cdot \rho_i)} \quad (7)$$

View Article Online
DOI: 10.1039/D5EB00188A

where w_i, V_i, and ρ_i are respectively the weight fraction (%), volume fraction (%) and density (g/cm^3) of component i, and j indicates all the components (HC, Sn, binder plus conductive carbon). The Sn weight % results to be 11.24 % for CC-Sn and 16.37 % for FC-Sn.

Finally, all the results obtained from different techniques are summarized in figure 4. For pycnometry an equation analogous to (6) was used. We can conclude that CC-Sn composites feature a higher Sn content, of the order of 18-20%, while FC-Sn has a lower content, approximately 13-15%. As TGA estimation appeared to be reliable, it was also performed on composites containing a higher amount of Sn, where a 1:1 HC:Sn weight ratio was targeted (labelled CC-Sn_50 and FC-Sn_50). The composites revealed a Sn amount of 26.87 ± 2.26 wt% and 23.89 ± 1.12 wt%, respectively. This result indicates that in laboratory scale spray drying the reactor size allows to get approximately a reaction yield (Sn content in composites vs. Sn content targeted) of 50%. Moreover, the morphology of CC allows a better incorporation of Sn than FC, since we constantly record a higher Sn amount for this hard carbon. As is often the case, it can be expected that industrial spray-dryers would achieve better yields due to their larger size and reduced surface.

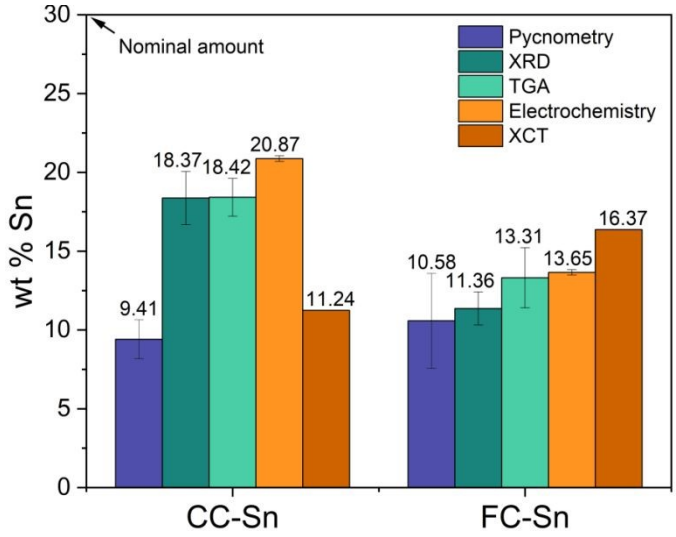

Figure 4: *weight % of Sn in the composites CC-Sn and FC-Sn determined with different techniques: pycnometry (purple), XRD with Si reference (dark aquamarine), TGA-MS (pale aquamarine), electrochemistry with diglyme electrolyte (orange) and x-ray microtomography (brown).*

Electrochemical results

Although it has been shown that the best electrolyte choices for metal anode electrodes are ether-based, for reasons of sustainability, cost, and adaptability to established Li-ion technology, we carried out electrochemical tests using conventional carbonate-based electrolytes. All our samples were tested in half cells vs sodium metal with 1M $NaPF_6$ in EC:PC as electrolyte, and the electrochemical results are reported in figure 5.

View Article Online
DOI: 10.1039/D5EB00188A

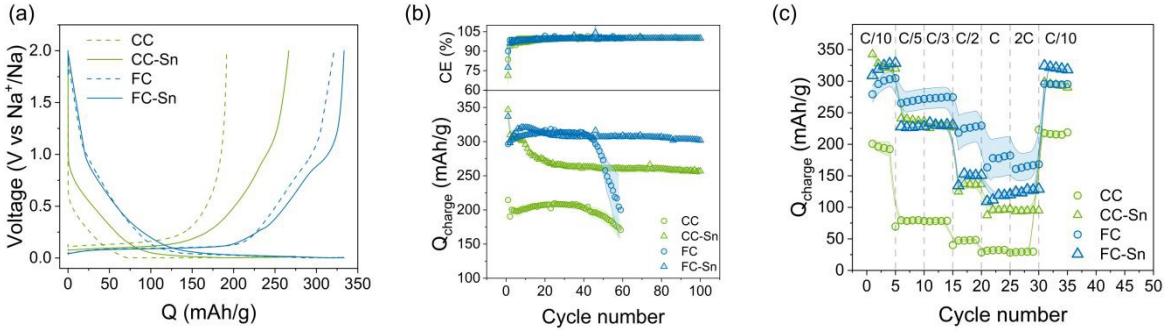

Figure 5: *(a) voltage profiles (10th cycle), (b) capacity retention (at C/10 rate) and CE and (c) rate capability tests of the samples. The composites show higher gravimetric capacity and better stability than the relative HC with increasing number of cycles. Testing is performed in half cells at 25 °C in the voltage window 0.002-2 V vs. Na+/Na.*

It has been shown that CMC and CMC:SBR binders perform better for HC materials than the conventional PVDF binder[38]. For this reason we firstly prepared electrodes of hard carbons with CMC:SBR binder using an AM:binder ratio equal to 95:5. We can confirm the successful usage of CMC:SBR for our FC electrode, while for CC the use of CMC:SBR was problematic and led to poor electrochemical performances (figure S14). To understand the origin of this phenomenon, we compared CC electrodes prepared with CMC:SBR and with PVdF by SEM. The SEM images are reported in figure S15, and since we used the same parameters for both, a comparison can be reasonably made. The effect of CMC:SBR binder (figure S15a) is to form a uniform thick (and likely passivating) layer on the surface of the electrode, while the surface of the electrode prepared with PVdF (figure S15b) looks thinner and accessible, and the CC particles are simply bound together. We then tried to optimize the amount of CMC:SBR in a CC electrode and identified the 96.5:3.5 formulation as enabling contact among the particles but not forming a passivating layer. However, the galvanostatic cycling test shows an unstable behaviour of the CC electrode, with a coulombic efficiency that overcomes the 100% value in several cycles (figure S14). On the other hand, the electrode formulation with PVdF shows a stable capacity behaviour even if providing a poorer performance. For this reason we choose to use the conventional PVdF binder for the couple CC and CC-Sn, preferring a stable electrode to better understand the effect of Sn in the composite material. Further work will be dedicated to the stabilization of CC with CMC:SBR binder and transferred then on the composite formulation. In figure 5a we show the voltage profile after the initial formation (10th cycle) of all our materials using PVdF binder in the electrode formulation for CC and CC-Sn and CMC:SBR for the couple FC and FC-Sn. In both cases, the contribution of Sn can be clearly seen in the shoulder present at 0.75 V vs Na+/Na during the charge step[28] [66]. The difference in capacity among the pristine HCs is reflected also in the composites and can be attributed to the size differences of closed pores in the materials and the roughness of the surfaces. FC and FC-Sn show larger closed pores than CC-Sn and CC, thus the higher the capacity of the plateau region at low voltage values. In figure 5b the capacity retention of the samples is reported. The improved capacity of CC-Sn compared to CC results in 55 mAh/g gained at the 30th cycle, and moreover the stability of CC is highly surpassed. Regarding the FC-Sn composite, despite a small improvement of the initial capacity (20 mAh/g more than FC), both samples perform similarly after 10 cycles. However the stability of FC has been clearly improved after Sn incorporation, as visible after 50 cycles. In figure 5c the rate capability test of our samples is shown. CC-Sn is superior to CC in every step, as a result of higher capacity, better stability and faster kinetics. For FC-Sn the situation is different, since it

View Article Online
DOI: 10.1039/D5EB00188A

provides more capacity than FC, but it appears to suffer from poor kinetics; FC indeed shows a better kinetics at higher C-rates. However, with larger error bars, while FC-Sn samples show more reproducible electrochemical behaviour. Overall, these rate capability test provide a first indication but need to be repeated in 3 electrodes cell configuration, which will be the object of future work.

Considering the density values obtained by pycnometry (Figure 2c), our composites provide higher volumetric capacity than HCs as well, resulting after 50 cycles in 549.26 mAh/cm^3 for CC-Sn and 910.38 mAh/cm^3 for FC-Sn (in comparison to 300.06 mAh/cm^3 for CC and 669.17 mAh/cm^3 for FC). These results confirm our approach leads to anode materials with increased volumetric energy density, considering that in LIBs a graphite-based anode provides 814 mAh/cm^3 (assuming a specific gravimetric capacity of 370 mAh/g and a density of 2.20 g/cm^3). Furthermore, we investigated the possibility to increase the active material percentage in the electrode, testing the formulations AM:conductive carbon:binder equal to 85:10:5 and 90:5:5. The capacity retention tests are reported in figure S16, clearly exhibiting worse performances in both cases with respect to the formulation 70:20:10. This demonstrates the importance of the conductive carbon additive when Sn is present in the electrodes. Indeed some of the Na-Sn alloys that form during the electrochemical discharge (e.g. NaSn) may have high melting point and low electrical conductivity[67], and do not guarantee the optimal working of the electrode. Once found that the conductive carbon is fundamental for the electrochemistry of the composites, we tested the samples with a higher Sn content, CC-Sn_50 and FC-Sn_50. The electrochemical tests are shown in figure S17, and they reveal a different behaviour for the two composites. Initially, both show higher capacity than CC-Sn and FC-Sn, as expected. After few cycles, however, FC-Sn_50 suffers from the higher Sn amount, resulting in a lower capacity than FC-Sn, likely due to Sn agglomeration and subsequent pulverization while cycling. On the other hand, surprisingly CC-Sn_50 shows higher capacity than CC-Sn, confirming that in this material the activation of Sn is more pronounced in terms of gained capacity through the morphology of CC in which Sn particles are embedded. This indicates that to increase the Sn content a suitable HC morphology is paramount. It should be noted, however, that the performances of CC-Sn_50 after 10 cycles are inferior to those of FC-Sn, indicating that for stable cycling at values close to 300 mAh/g large amounts of Sn are not required.

Finally we tested the effect of the spray-dry process (without Sn) on HCs' electrochemistry, as shown in figure S18. The water-based spray-dry process clearly induces degradation in the performance, as both the gravimetric capacity and the initial coulombic efficiency (ICE) are lower than pristine HC. This behaviour is likely related to the increase of surface area observed during the spray-dry process [41], as shown by BET measurements. The presence of Sn assumes an important role in the composites CC-Sn and FC-Sn: even though we observe a decrease in ICE from 83.7 % to 71.2 % for the couple CC/CC-Sn and from 89.9 % to 77.5 % in the couple FC/FC-Sn, the subsequent cycling stability is significantly higher when Sn is present. Moreover, the difficult cell balancing due to lower ICE can be eventually overcome by alternative strategies like anode presodiation or addition of sacrificial salt.

Sodiation Mechanism by Operando XRD and ex Situ SEM/EDX

View Article Online
DOI: 10.1039/D5EB00188A

Synchrotron x-ray powder diffraction (SXRPD) is one of the most powerful techniques for the study of complex phenomena that occur in battery processes[68]. Following the transformation of the electrode materials during coulometric titration gives fundamental information regarding the structural changes and phase evolution. Sn as negative electrode material has been investigated in literature via operando XRD, and usually not all the alloys suggested by the Na-Sn binary phase diagram are observed to form[69] [18]. One would expect to observe the evolution of Sn, $NaSn_5$, NaSn, Na_9Sn_4 and $Na_{15}Sn_4$ phases, but actually only the high sodium content phases are observed during the electrochemical discharge (i.e. typically Na_9Sn_4 and $Na_{15}Sn_4$) [69] [70] [33]. It is suggested that the remaining phases are kinetically hard to crystallize. More details are presented in the study of Stratford et al. [71], where some other structures are proposed as intermediate Na-Sn phases, based on NMR and PDF data . The same challenge has been reported by Palaniselvam et al.[72], where the operando XRD of Sn has been investigated in tin-carbon composite electrodes. Here, the authors confirmed the lack of some expected phases by showing the mismatching of the in situ patterns with the reference ones. Since we are interested in confirming the activity of Sn in our composites as well as in verifying the results reported in literature, we decided to carry out a synchrotron x-ray powder diffraction (SXRPD) measurement on the composite CC-Sn which has a higher Sn content. In figure 6a we show the operando SXRPD of CC-Sn at 50 °C during the electrochemical discharge at C/10, including the voltage profile and the dQ/dV curve in figure 6b. The higher temperature was selected to enhance the slow kinetics of Sn phases formation.

Figure 6: Operando SXRPD of CC-Sn at 50 °C and C/10 (a) and the corresponding voltage profile and dQ/dV curve (b). We highlight the patterns corresponding to observed intermediate crystalline phases. The peak marked with * corresponds to Al from current collector. c) ex situ SEM and EDX (d) of CC-Sn after a full discharge at 25 °C.

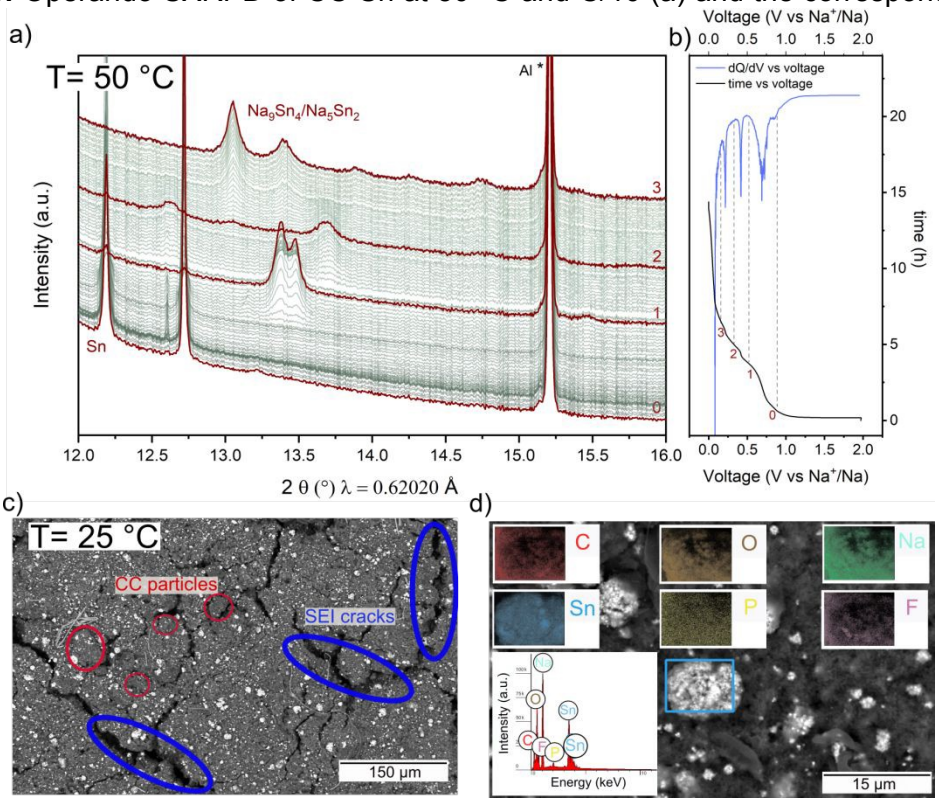

At OCV, we can clearly identify the peaks of Sn. At the beginning of the electrochemical discharge we observe a first voltage plateau at 0.7 V. Below 0.5 V the formation of Na-Sn alloys becomes visible. The dQ/dV plot (figure 6b) allows to identify the processes encountered in the discharge curve, as we can match its peaks with the plateau in the voltage

View Article Online
DOI: 10.1039/D5EB00188A

profile, and the minima with the stabilized intermediate phases. The reactions start with the initial phase marked “0” corresponding to Sn metal and leading to the first effective plateau, at the end of which the first Na_xSn ($0<x<1$) intermediate phase forms, marked “1”, revealed by the disappearance of the Sn metal peaks in the SXRPD pattern, and the formation of a peak doublet around 13.2-13.5°. Based on the electrochemistry result, this phase corresponds to $Na_{1.08}Sn$. The next plateau leads to the formation of a second unidentified phase “2” characterized by a clear reflection at 13.7° and nominally corresponding to $Na_{1.80}Sn$. Presently we cannot attribute these intermediate phases to any known structure and the confirmation of the stoichiometry suggested by the electrochemistry will be subject of future work. Finally, the last plateau generates a last crystalline phase with a main reflection at 13° (marked “3”). Once reached 0.002 V we get a capacity of 563.45 mAh/g, that can be divided into the contribution of CC and Sn. Since we expect Sn to contribute for roughly 19 % of the total capacity, we assume it provides 107.06 mAh/g, that results to be the equivalent of the capacity provided by an electrode containing 19 % of $Na_{4.99}Sn_2$. Our operando pattern at end of discharge matches well with the Na_5Sn_2 phase, as can be seen also in figure S19. This crystalline phase has been observed in operando studies on Sn foil and film[73] [74] and powder electrodes [71] in carbonate electrolytes, while in studies that used ether electrolytes it is mostly replaced by the Na_9Sn_4 phase. It has been shown that both crystalline phases Na_5Sn_2 and Na_9Sn_4 electrochemically crystallize in the space group $R\bar{3}m$, therefore a solid solution with composition $Na_{5-x}Sn_2$ is formed, starting from Na_9Sn_4 that gradually transforms in Na_5Sn_2 with the increase in occupancy of one Na site[75] [71]. Therefore it is impossible to unequivocally identify the final phase observed in Figure 6, but the electrochemical results indicate it is close to the Na_5Sn_2 phase. To further confirm this, we conducted ex situ SEM-EDX measurements on a composite anode that was fully discharged in a half cell at 25 °C. Figure 6c shows the SEM image of the electrode CC-Sn, and with the backscattering detector it’s easy to identify the shiny particles that correspond to the Na-Sn alloys (see figure S20c for the FC-Sn electrode as well). Indeed, when the SED detector is used no clear difference among the HC and the Na-Sn alloy particles is present (figure S20a, S20b). After the electrochemical discharge, the SEI has been formed and the expansion of Sn, once it has reacted with Na, is translated in the formation of some cracks on the surface of the electrode. In figure 6d we report the EDX analysis of the same electrode, with a focus on the shiny particles in the attempt of quantifying their elemental composition. As we expect, the EDX reveals the presence of C, Sn, Na and O, with some traces of P and F coming from the electrolyte. All these elements are uniformly distributed on the target particle, and we were able to fit the EDX spectrum for the elemental quantification. Based on the atomic weight of the elements of interest and considering that our measurement is not provided of a standard for accurate EDX elemental quantification, we expect a bigger error in the estimation of Na amount than for Sn, so we performed the analysis on different areas of the electrode for a more reliable statistic. Repeating the measurement on 3 particles, ex situ analysis confirms a wt% ratio of Na/Sn equal to 2.4 ± 0.2 for CC-Sn and 3.1 ± 0.4 for FC-Sn, and these results confirm the non-complete sodiation of Sn, since the $Na_{3.75}Sn$ phase ($Na_{15}Sn_4$) has not formed. The incomplete sodiation of tin in this work, so the absence of the high-sodium-content phase $Na_{15}Sn_4$ could be ascribed to the presence of HC, that shows its most significant contribution in the long plateau at low voltage values. The fact that the HC capacity observed in this operando experiment is higher than the values observed in half cells is most likely due to the stronger electrolyte degradation at 50 °C at the low voltage of the HC plateau. The limited Sn sodiation during the electrochemical discharge (occurring primarily at higher voltage than the HC plateau) offers a recognizable advantage in the system as we experience an increase in the gravimetric capacity of the composite without incurring into huge electrode volume changes that is expected to be confined to 247 % compared to 388 % reported for $Na_{15}Sn_4$ phase [20], thus explaining the noticeable stability of our composites.

View Article Online
DOI: 10.1039/D5EB00188A

Comparison of spray-dry with other methods of Sn incorporation

In order to prove the superiority of spray drying synthesis over conventional routes, we also synthesized additional composites starting from the same chemicals. First of all, we tried to simply mix HC with Sn nanoparticles in a mortar, and we hand-mixed the blend for 10 minutes. We prepared two couples of batches, where the Sn amount was varied. For the first batch we used 30 wt% of Sn, as we did for the spray drying, and for the second batch we used 15 wt% Sn, as it is a closer value to the amount of Sn we effectively obtained in our spray-dry composites (Figure 4). We labelled then the samples CC-Sn/mortar30 and FC-Sn/mortar30 for the samples with 30 Sn wt%, and the samples CC-Sn/mortar15 and FC-Sn/mortar15 when the Sn wt% is 15. Furthermore, we synthesized another batch via mechanical ball milling, as it is reported to be a common synthesis route to prepare composite anode materials [28]. Ball milling guarantees an energetic mixing of the precursor, offering the good comparison in our study; we used 15 wt% Sn for this preparation. We labelled these last samples as CC-Sn/ballmill15 and FC-Sn/ballmill15. We confirmed the expected Sn amount in all the new samples with TGA (Figure S21). This time we exactly know the amount of Sn that we expect to be integrated in the samples, since the loss of material is negligible compared to spray drying (especially for the hand-mixed samples). This further highlights the feasibility of TGA as a technique to determine the unknown amount of Sn in composites materials. We tested the new materials electrochemically in the same configuration as the spray dried samples, and their electrochemical performance is shown in figure S22. In the first cycle, the high Sn content samples (CC-Sn/mortar30 and FC-Sn/mortar30) show the highest capacity due to the Sn contribution during the sodiation process, but then they show a quick capacity fade (figure S22c). This can be explained by the huge volume expansion of Sn during the sodiation process, that brings to SEI continuous destruction cycle by cycle and to cell failure[15] [26]. The low Sn amount samples prepared in the mortar show poorer initial capacity compared to the high Sn amount ones, as expected (figure S22a). Moreover, the insufficient HC and Sn mixing does not result in any improvement of capacity but in a discontinuous and poorly reproducible behaviour that leads to capacity fade, once the 50th cycle has been reached (as for pristine HCs). Regarding the ball milled samples (figure S22b), in the sample CC-Sn/ballmill15 we record a capacity comparable to CC-Sn at the 20th cycle, but a capacity drop afterwards. For the FC-Sn/ballmill15 sample we even record a lower capacity than HCs. This feature can be explained by considering the pulverization of HC induced by hard ball milling, that does not only decrease the particle size but also modify the internal structure made of micropores[52]. The low Sn content then is not sufficient to compensate for this lack of capacity. The electrochemical results of all composites are gathered in Figure 7, which clearly demonstrate how HC-Sn composites made by spray drying may be a promising alternative to provide stable cycling above 300 mAh/g, and with improved volumetric performances as well.

View Article Online
DOI: 10.1039/D5EB00188A

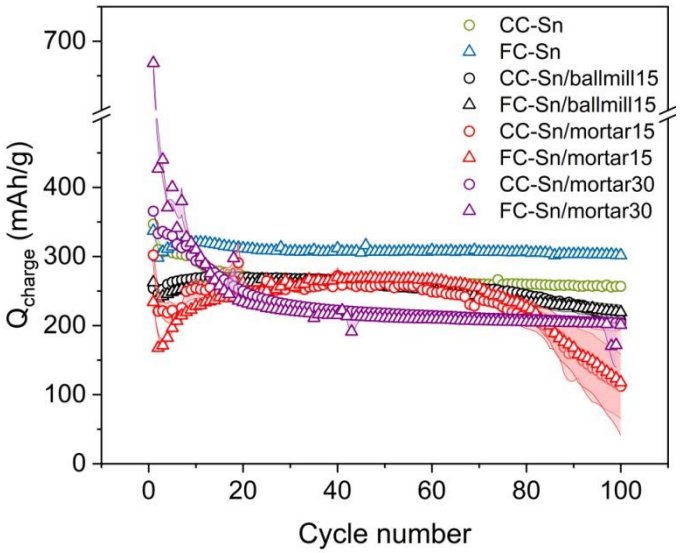

Figure 7: *Electrochemical performance of spray dried samples vs composites made by other methods (hand ground and ball milled). Here we report samples prepared with 30 and 15 Sn wt% in a mortar and the samples prepared with 15 Sn wt% in ball milling jars.*

Conclusion

In our work we synthesized HC-Sn composites by spray drying. Their physical properties were accurately tested by a combination of Raman, SAXS, SEM and BET, and their electrochemical performances were tested in Na half cells. We faced the problem of determining the Sn amount content in our composites, and we successfully benchmarked a range of different techniques, showing that TGA, electrochemical measurements in diglyme electrolytes and XRD with a proper reference material give comparable and trustworthy results. Based on this, we found our samples contain on average close to 15 or 25 wt% Sn depending on the initial Sn amount. The structural and morphological effects of spray drying synthesis were determined, taking into account the amorphization of Sn nanoparticles and the modification of surface area of HC materials. We confirm that these parameters and the mesostructure modification after Sn incorporation are the main reason for the improvement in capacity with respect to HC, since the nanostructure of HC analysed with SAXS and Raman shows minor differences after spraying. The electrochemical effect of Sn was determined via operando synchrotron XRD, revealing the formation of two intermediate phases before finally the solid solution $Na_{5-x}Sn_2$ is obtained, that increases hard carbon capacity without incurring in dramatic volume expansion typical of high-sodium-content Na-Sn alloys. These results are also confirmed by ex situ SEM and EDX analysis on electrodes recovered at the end of electrochemical discharge. Moreover we verified the importance of an optimal electrode formulation, highlighting that a small difference in binder percentage can affect the electrochemistry performance of the materials. Different Sn contents in the composites were tested, revealing that a higher Sn content only gives an improvement of electrochemical performances for appropriate HC morphologies, hence we report an improvement of CC-Sn_50 on CC-Sn and a deterioration of FC-Sn_50 on FC-Sn. We also compared the electrochemical performance of our spray dried samples with other reference materials, synthesized with the same reactants but using hand mixing and ball milling. Overall, our spray dried materials show the best capacity retention, since we performed an effective mixing of the precursors without modifying the internal structure of HC. As a result, the HC matrix successfully helps in mitigating Sn nanoparticles expansion and pulverization, while retaining

View Article Online
DOI: 10.1039/D5EB00188A

its sodium storage capacity. The increase of effective surface area after spraying also contributes to the improved performances. In this context, the morphology of HC plays a fundamental role, as in CC-Sn we observe a more noticeable increase in gravimetric capacity compared to CC, due to the favourable presence of roughness in the CC surface that allows Sn storage, as confirmed by SAXS scattering length value and SEM. While for FC-Sn, which shows less surface roughness, we observe a smaller difference in electrochemical performance compared to FC. Nonetheless, FC-Sn is the best composite in terms of gravimetric capacity and especially capacity retention, which is consistently above 300 mAh/g after 100 cycles, and moreover it has shown to surpass the volumetric capacity of graphite in LIBs. In any case, it should be noted that due to the increased density, for both composite negative electrodes we observe an increase in volumetric capacity (and energy) as well. This represents a potential solution to a fundamental problem in commercial Na-ion batteries, making spray drying synthesis a valid alternative to other methods to increase gravimetric and especially volumetric performances of negative electrode materials.

Acknowledgements

The authors acknowledge the contribution of the following researchers at University of Bayreuth: Dr. Holger Schmalz at the Keylab “Synthesis and Molecular Characterization” (Prof. Dr. Andreas Greiner) for Raman spectroscopy measurements, Dennis Bieg at the BayBatt Keylab for pycnometry measurements, Dr. Ulrich Mansfeld at the Keylab “Electron and Optical Microscopy” (Prof. Dr. Hans-Werner Schmidt) for the SEM images of electrode samples, Dr. Sabine Rosenfeldt at the Keylab “Mesoscale Characterization: Scattering Techniques” (Prof. Dr. Markus Retsch, Jun. Prof. Dr. Anna Schenk) for SAXS measurements, Michael Thelen and Lukas Federer at the Chair of Inorganic Colloids for Electrochemical Energy storage (Prof. Dr. Josef Breu) for BET measurements. The help of Dr. Stefan Seidlmayer for SAXS fitting is kindly acknowledged. The authors acknowledge ALBA for the allocation of SXRPD measurements at the beamline MSPD (Proposal ID: 2024028147). Funded by the European Union (ERC StG 4SBATT, project101039399). Views and opinions expressed are however those of the author(s) only and do not necessarily reflect those of the European Union or the European Research Council Executive Agency. Neither the European Union nor the granting authority can be held responsible for them. Support by the BayBatt Cell Technology Center is gratefully acknowledged, funded by the Deutsche Forschungsgemeinschaft (DFG, German Research Foundation) - INST 91/452-1 LAGG.

Bibliography

[1] N. Yabuuchi, K. Kubota, M. Dahbi, S. Komaba, ““Research Development on Sodium-Ion Batteries,”” *Chem. Rev.* **2014**, *114*, 11636–11682.
[2] L. W. Shacklette, T. R. Jow, L. Townsend, ““Rechargeable Electrodes from Sodium Cobalt Bronzes,”” *J. Electrochem. Soc.* **1988**, *135*, 2669.
[3] K. Kubota, M. Dahbi, T. Hosaka, S. Kumakura, S. Komaba, ““Towards K-Ion and Na-Ion Batteries as ‘Beyond Li-Ion,’”” *Chem. Rec.* **2018**, *18*, 459–479.
[4] C. Delmas, ““Sodium and Sodium-Ion Batteries: 50 Years of Research,”” *Adv. Energy Mater.* **2018**, *8*, 1703137.
[5] P. K. Nayak, L. Yang, W. Brehm, P. Adelhelm, ““From Lithium-Ion to Sodium-Ion Batteries: Advantages, Challenges, and Surprises,”” *Angew. Chem. Int. Ed.* **2018**, *57*, 102–120.

[6] A. Nekahi, M. Dorri, M. Rezaei, M. D. Bouguern, A. K. Madikere Raghunatha Reddy, X. Li, S. Deng, K. Zaghib, ""Comparative Issues of Metal-Ion Batteries toward Sustainable Energy Storage: Lithium vs. Sodium,"" *Batteries* **2024**, *10*, 279.
[7] ""Why TIAMAT,"" "Why TIAMAT," can be found under https://www.tiamat-energy.com/, **n.d.**
[8] C. Matei Ghimbeu, A. Beda, B. Réty, H. El Marouazi, A. Vizintin, B. Tratnik, L. Simonin, J. Michel, J. Abou-Rjeily, R. Dominko, ""Review: Insights on Hard Carbon Materials for Sodium-Ion Batteries (SIBs): Synthesis – Properties – Performance Relationships,"" *Adv. Energy Mater.* **2024**, *14*, 2303833.
[9] C. Vaalma, D. Buchholz, M. Weil, S. Passerini, ""A cost and resource analysis of sodium-ion batteries,"" *Nat. Rev. Mater.* **2018**, *3*, 18013.
[10] A. Magasinski, P. Dixon, B. Hertzberg, A. Kvit, J. Ayala, G. Yushin, ""High-performance lithium-ion anodes using a hierarchical bottom-up approach,"" *Nat. Mater.* **2010**, *9*, 353–358.
[11] A. D. Roberts, X. Li, H. Zhang, ""Porous carbon spheres and monoliths: morphology control, pore size tuning and their applications as Li-ion battery anode materials,"" *Chem Soc Rev* **2014**, *43*, 4341–4356.
[12] H. Tian, F. Xin, X. Wang, W. He, W. Han, ""High capacity group-IV elements (Si, Ge, Sn) based anodes for lithium-ion batteries,"" *J. Materiomics* **2015**, *1*, 153–169.
[13] M. N. Obrovac, V. L. Chevrier, ""Alloy Negative Electrodes for Li-Ion Batteries,"" *Chem. Rev.* **2014**, *114*, 11444–11502.
[14] M.-S. Balogun, Y. Luo, W. Qiu, P. Liu, Y. Tong, ""A review of carbon materials and their composites with alloy metals for sodium ion battery anodes,"" *Carbon* **2016**, *98*, 162–178.
[15] S.-M. Zheng, Y.-R. Tian, Y.-X. Liu, S. Wang, C.-Q. Hu, B. Wang, K.-M. Wang, ""Alloy anodes for sodium-ion batteries,"" *Rare Met.* **2021**, *40*, 272–289.
[16] G. Yang, P. R. Ilango, S. Wang, M. S. Nasir, L. Li, D. Ji, Y. Hu, S. Ramakrishna, W. Yan, S. Peng, ""Carbon-Based Alloy-Type Composite Anode Materials toward Sodium-Ion Batteries,"" *Small* **2019**, *15*, 1900628.
[17] Y. Kim, K. Ha, S. M. Oh, K. T. Lee, ""High-Capacity Anode Materials for Sodium-Ion Batteries,"" *Chem. – Eur. J.* **2014**, *20*, 11980–11992.
[18] Z. Li, J. Ding, D. Mitlin, ""Tin and Tin Compounds for Sodium Ion Battery Anodes: Phase Transformations and Performance,"" *Acc. Chem. Res.* **2015**, *48*, 1657–1665.
[19] Y. Lee, H. Lim, S.-O. Kim, H.-S. Kim, K. J. Kim, K.-Y. Lee, W. Choi, ""Thermal stability of Sn anode material with non-aqueous electrolytes in sodium-ion batteries,"" *J. Mater. Chem. A* **2018**, *6*, 20383–20392.
[20] H. Kim, J. C. Kim, M. Bianchini, D. Seo, J. Rodriguez-Garcia, G. Ceder, ""Recent Progress and Perspective in Electrode Materials for K-Ion Batteries,"" *Adv. Energy Mater.* **2018**, *8*, 1702384.
[21] F. Xin, M. S. Whittingham, ""Challenges and Development of Tin-Based Anode with High Volumetric Capacity for Li-Ion Batteries,"" *Electrochem. Energy Rev.* **2020**, *3*, 643–655.
[22] J. Hassoun, G. Derrien, S. Panero, B. Scrosati, ""A Nanostructured Sn–C Composite Lithium Battery Electrode with Unique Stability and High Electrochemical Performance,"" *Adv. Mater.* **2008**, *20*, 3169–3175.
[23] B. Guo, J. Shu, K. Tang, Y. Bai, Z. Wang, L. Chen, ""Nano-Sn/hard carbon composite anode material with high-initial coulombic efficiency,"" *J. Power Sources* **2008**, *177*, 205–210.
[24] G. Derrien, J. Hassoun, S. Panero, B. Scrosati, ""Nanostructured Sn–C Composite as an Advanced Anode Material in High-Performance Lithium-Ion Batteries,"" *Adv. Mater.* **2007**, *19*, 2336–2340.
[25] N. Zhang, Q. Zhao, X. Han, J. Yang, J. Chen, ""Pitaya-like Sn@C nanocomposites as high-rate and long-life anode for lithium-ion batteries,"" *Nanoscale* **2014**, *6*, 2827–2832.
[26] W. Luo, F. Shen, C. Bommier, H. Zhu, X. Ji, L. Hu, ""Na-Ion Battery Anodes: Materials and Electrochemistry,"" *Acc. Chem. Res.* **2016**, *49*, 231–240.

[27] Y. Li, S. Xu, X. Wu, J. Yu, Y. Wang, Y.-S. Hu, H. Li, L. Chen, X. Huang, ""Amorphous monodispersed hard carbon micro-spherules derived from biomass as a high performance negative electrode material for sodium-ion batteries,"" *J. Mater. Chem. A* **2015**, *3*, 71–77.
[28] T. Palaniselvam, M. Goktas, B. Anothumakkool, Y. Sun, R. Schmuch, L. Zhao, B. Han, M. Winter, P. Adelhelm, ""Sodium Storage and Electrode Dynamics of Tin–Carbon Composite Electrodes from Bulk Precursors for Sodium-Ion Batteries,"" *Adv. Funct. Mater.* **2019**, *29*, 1900790.
[29] S. Müllner, T. Held, A. Schmidt-Rodenkirchen, T. Gerdes, C. Roth, ""Reactive Spray Drying as a One-Step Synthesis Approach towards Si/rGO Anode Materials for Lithium-Ion Batteries,"" *J. Electrochem. Soc.* **2021**, *168*, 120545.
[30] H. Ying, S. Zhang, Z. Meng, Z. Sun, W.-Q. Han, ""Ultrasmall Sn nanodots embedded inside N-doped carbon microcages as high-performance lithium and sodium ion battery anodes,"" *J. Mater. Chem. A* **2017**, *5*, 8334–8342.
[31] M. D. L. Garayt, L. Zhang, Y. Zhang, M. C. Obialor, J. Deshmukh, Y. Xing, C. Yang, M. Metzger, J. R. Dahn, ""Practical Alloy-Based Negative Electrodes for Na-ion Batteries,"" *J. Electrochem. Soc.* **2024**, *171*, 070523.
[32] M. D. L. Garayt, M. Obialor, I. Monchesky, A. George, S. Yu, B. Rutherford, M. Metzger, J. R. Dahn, ""Restructuring of Sodium-Lead Alloys during Charge-Discharge Cycling in Sodium-Ion Batteries,"" *J. Electrochem. Soc.* **2024**, , DOI 10.1149/1945-7111/ad9bf0.
[33] B. Zhang, G. Rousse, D. Foix, R. Dugas, D. A. D. Corte, J. Tarascon, ""Microsized Sn as Advanced Anodes in Glyme-Based Electrolyte for Na-Ion Batteries,"" *Adv. Mater.* **2016**, *28*, 9824–9830.
[34] F. Cheng, J. Hu, W. Zhang, B. Guo, P. Yu, X. Sun, J. Peng, ""Reviving ether-based electrolytes for sodium-ion batteries,"" *Energy Environ. Sci.* **2025**, 10.1039.D5EE00725A.
[35] R. G. Houdeville, A. Missyul, V. Fuentes, M. M. P. Moline, F. Farre, J. B. Gonzalez, M. R. Palacin, F. Fauth, ""Method—Setups and Protocols for Operando Batteries Experiments at Variable Temperatures Applied to Ca_x TiS_2 and Na_{3-x} V_2 $(PO_4)_3$,"" *J. Electrochem. Soc.* **2024**, *171*, 020533.
[36] R. Bardestani, G. S. Patience, S. Kaliaguine, ""Experimental methods in chemical engineering: specific surface area and pore size distribution measurements—BET, BJH, and DFT,"" *Can. J. Chem. Eng.* **2019**, *97*, 2781–2791.
[37] H. Chen, M. Ling, L. Hencz, H. Y. Ling, G. Li, Z. Lin, G. Liu, S. Zhang, ""Exploring Chemical, Mechanical, and Electrical Functionalities of Binders for Advanced Energy-Storage Devices,"" *Chem. Rev.* **2018**, *118*, 8936–8982.
[38] K. Kubota, S. Komaba, ""Review—Practical Issues and Future Perspective for Na-Ion Batteries,"" *J. Electrochem. Soc.* **2015**, *162*, A2538–A2550.
[39] C. Matei Ghimbeu, J. Górka, V. Simone, L. Simonin, S. Martinet, C. Vix-Guterl, ""Insights on the Na+ ion storage mechanism in hard carbon: Discrimination between the porosity, surface functional groups and defects,"" *Nano Energy* **2018**, *44*, 327–335.
[40] V. Simone, A. Boulineau, A. De Geyer, D. Rouchon, L. Simonin, S. Martinet, ""Hard carbon derived from cellulose as anode for sodium ion batteries: Dependence of electrochemical properties on structure,"" *J. Energy Chem.* **2016**, *25*, 761–768.
[41] Y. Yang, C. Wu, X. He, J. Zhao, Z. Yang, L. Li, X. Wu, L. Li, S. Chou, ""Boosting the Development of Hard Carbon for Sodium-Ion Batteries: Strategies to Optimize the Initial Coulombic Efficiency,"" *Adv. Funct. Mater.* **2024**, *34*, 2302277.
[42] D. Chen, W. Zhang, K. Luo, Y. Song, Y. Zhong, Y. Liu, G. Wang, B. Zhong, Z. Wu, X. Guo, ""Hard carbon for sodium storage: mechanism and optimization strategies toward commercialization,"" *Energy Environ. Sci.* **2021**, *14*, 2244–2262.
[43] F. Xie, Z. Xu, Z. Guo, M.-M. Titirici, ""Hard carbons for sodium-ion batteries and beyond,"" *Prog. Energy* **2020**, *2*, 042002.

[44] V. Surendran, R. K. Hema, M. S. O. Hassan, V. Vijayan, M. M. Shaijumon, ""Open or Closed? Elucidating the Correlation between Micropore Nature and Sodium Storage Mechanisms in Hard Carbon,"" *Batter. Supercaps* **2022**, *5*, e202200316.
[45] K. Wang, F. Sun, H. Wang, D. Wu, Y. Chao, J. Gao, G. Zhao, ""Altering Thermal Transformation Pathway to Create Closed Pores in Coal-Derived Hard Carbon and Boosting of Na^+ Plateau Storage for High-Performance Sodium-Ion Battery and Sodium-Ion Capacitor,"" *Adv. Funct. Mater.* **2022**, *32*, 2203725.
[46] L. Zhou, Y. Cui, P. Niu, L. Ge, R. Zheng, S. Liang, W. Xing, ""Biomass-derived hard carbon material for high-capacity sodium-ion battery anode through structure regulation,"" *Carbon* **2025**, *231*, 119733.
[47] E. O. Eren, E. Senokos, Z. Song, B. Mondal, A. Perju, T. Horner, E. B. Yılmaz, E. Scoppola, P.-L. Taberna, P. Simon, M. Antonietti, P. Giusto, ""Hard carbon from a sugar derivative for next-generation sodium-ion batteries,"" *Mater. Horiz.* **2025**, *12*, 886–898.
[48] L. Kitsu Iglesias, E. N. Antonio, T. D. Martinez, L. Zhang, Z. Zhuo, S. J. Weigand, J. Guo, M. F. Toney, ""Revealing the Sodium Storage Mechanisms in Hard Carbon Pores,"" *Adv. Energy Mater.* **2023**, *13*, 2302171.
[49] H. Au, H. Alptekin, A. C. S. Jensen, E. Olsson, C. A. O'Keefe, T. Smith, M. Crespo-Ribadeneyra, T. F. Headen, C. P. Grey, Q. Cai, A. J. Drew, M.-M. Titirici, ""A revised mechanistic model for sodium insertion in hard carbons,"" *Energy Environ. Sci.* **2020**, *13*, 3469–3479.
[50] X. Liu, M. Zhang, X. Wang, Y. Peng, Y. Liu, S. Ullah, Z. Duan, W. Gao, B. Song, M. Wei, J. He, Z. Li, Y. Wu, ""Evidence of Quasi-Na Metallic Clusters in Sodium Ion Batteries through In Situ X-Ray Diffraction,"" *Adv. Mater.* **2025**, *37*, 2410673.
[51] Z. Wang, X. Feng, Y. Bai, H. Yang, R. Dong, X. Wang, H. Xu, Q. Wang, H. Li, H. Gao, C. Wu, ""Probing the Energy Storage Mechanism of Quasi-Metallic Na in Hard Carbon for Sodium-Ion Batteries,"" *Adv. Energy Mater.* **2021**, *11*, 2003854.
[52] I. K. Ilic, K. Schutjajew, W. Zhang, M. Oschatz, ""Changes of porosity of hard carbons during mechanical treatment and the relevance for sodium-ion anodes,"" *Carbon* **2022**, *186*, 55–63.
[53] L. A. Feigin, D. I. Svergun, G. W. Taylor, "*General Principles of Small-Angle Diffraction*," in *Struct. Anal. Small-Angle X-Ray Neutron Scatt.* (Eds.: L.A. Feigin, D.I. Svergun, G.W. Taylor), Springer US, Boston, MA, **1987**, pp. 25–55.
[54] O. Glatter, "*Chapter 2 - General Theorems and Special Cases*," in *Scatt. Methods Their Appl. Colloid Interface Sci.* (Ed.: O. Glatter), Elsevier, **2018**, pp. 19–32.
[55] A. C. Ferrari, J. Robertson, ""Interpretation of Raman spectra of disordered and amorphous carbon,"" *Phys. Rev. B* **2000**, *61*, 14095–14107.
[56] A. C. Ferrari, J. Robertson, ""Raman spectroscopy of amorphous, nanostructured, diamond–like carbon, and nanodiamond,"" *Philos. Trans. R. Soc. Lond. Ser. Math. Phys. Eng. Sci.* **2004**, *362*, 2477–2512.
[57] C. Hu, S. Sedghi, A. Silvestre-Albero, G. G. Andersson, A. Sharma, P. Pendleton, F. Rodríguez-Reinoso, K. Kaneko, M. J. Biggs, ""Raman spectroscopy study of the transformation of the carbonaceous skeleton of a polymer-based nanoporous carbon along the thermal annealing pathway,"" *Carbon* **2015**, *85*, 147–158.
[58] C. Wu, Y. Yang, Y. Li, X. He, Y. Zhang, W. Huang, Q. Chen, X. Liu, S. Chen, Q. Gu, L. Li, S. C. Smith, X. Tan, Y. Yu, X. Wu, S. Chou, ""Unraveling the structure–performance relationship in hard carbon for sodium-ion battery by coupling key structural parameters,"" *Energy Environ. Sci.* **2025**, 10.1039.D5EE00278H.
[59] A. Sadezky, H. Muckenhuber, H. Grothe, R. Niessner, U. Pöschl, ""Raman microspectroscopy of soot and related carbonaceous materials: Spectral analysis and structural information,"" *Carbon* **2005**, *43*, 1731–1742.
[60] M. Curcio, S. Brutti, L. Caripoti, A. De Bonis, R. Teghil, ""Laser Irradiation of a Bio-Waste Derived Carbon Unlocks Performance Enhancement in Secondary Lithium Batteries,"" *Nanomaterials* **2021**, *11*, 3183.

[61] X. Yao, Y. Ke, W. Ren, X. Wang, F. Xiong, W. Yang, M. Qin, Q. Li, L. Mai, ""Defect-Rich Soft Carbon Porous Nanosheets for Fast and High-Capacity Sodium-Ion Storage,"" *Adv. Energy Mater.* **2019**, *9*, 1803260.
[62] C. Marino, J. Cabanero, M. Povia, C. Villevieille, ""Biowaste Lignin-Based Carbonaceous Materials as Anodes for Na-Ion Batteries,"" *J. Electrochem. Soc.* **2018**, *165*, A1400–A1408.
[63] H. Jang, I. Hasa, H. Kim, Y. Hwa, Y.-W. Byeon, R. Kostecki, H. Kim, ""Exploring the Storage Mechanism of Alkali Ions in Non-Graphitic Hard Carbon Anodes,"" *J. Electrochem. Soc.* **2023**, *170*, 090538.
[64] T. Zhao, M. A. Kraft, W. G. Zeier, ""Synthesis-Controlled Polymorphism and Anion Solubility in the Sodium-Ion Conductor $Na_3InCl_{6-x}Br_x$ ($0 \le x \le 2$),"" *Inorg. Chem.* **2023**, *62*, 11737–11745.
[65] Y. Xu, Q. Liu, Y. Zhu, Y. Liu, A. Langrock, M. R. Zachariah, C. Wang, ""Uniform Nano-Sn/C Composite Anodes for Lithium Ion Batteries,"" *Nano Lett.* **2013**, *13*, 470–474.
[66] Y. Liu, N. Zhang, L. Jiao, J. Chen, ""Tin Nanodots Encapsulated in Porous Nitrogen-Doped Carbon Nanofibers as a Free-Standing Anode for Advanced Sodium-Ion Batteries,"" *Adv. Mater.* **2015**, *27*, 6702–6707.
[67] J. M. Stratford, M. Mayo, P. K. Allan, O. Pecher, O. J. Borkiewicz, K. M. Wiaderek, K. W. Chapman, C. J. Pickard, A. J. Morris, C. P. Grey, ""Investigating Sodium Storage Mechanisms in Tin Anodes: A Combined Pair Distribution Function Analysis, Density Functional Theory, and Solid-State NMR Approach,"" *J. Am. Chem. Soc.* **2017**, *139*, 7273–7286.
[68] M. Bianchini, V. Lacivita, D.-H. Seo, H. Kim, ""Advances and challenges in multiscale characterizations and analyses for battery materials,"" *J. Mater. Res.* **2022**, *37*, 3113–3129.
[69] L. D. Ellis, T. D. Hatchard, M. N. Obrovac, ""Reversible Insertion of Sodium in Tin,"" *J. Electrochem. Soc.* **2012**, *159*, A1801–A1805.
[70] C. Kim, H. Kim, M. K. Sadan, M. Jeon, G. Cho, J. Ahn, K. Kim, K. Cho, H. Ahn, ""Development and Evaluation of Sn Foil Anode for Sodium-Ion Batteries,"" *Small* **2021**, *17*, 2102618.
[71] J. M. Stratford, M. Mayo, P. K. Allan, O. Pecher, O. J. Borkiewicz, K. M. Wiaderek, K. W. Chapman, C. J. Pickard, A. J. Morris, C. P. Grey, ""Investigating Sodium Storage Mechanisms in Tin Anodes: A Combined Pair Distribution Function Analysis, Density Functional Theory, and Solid-State NMR Approach,"" *J. Am. Chem. Soc.* **2017**, *139*, 7273–7286.
[72] T. Palaniselvam, M. Goktas, B. Anothumakkool, Y. Sun, R. Schmuch, L. Zhao, B. Han, M. Winter, P. Adelhelm, ""Sodium Storage and Electrode Dynamics of Tin–Carbon Composite Electrodes from Bulk Precursors for Sodium-Ion Batteries,"" *Adv. Funct. Mater.* **2019**, *29*, 1900790.
[73] L. Baggetto, P. Ganesh, R. P. Meisner, R. R. Unocic, J.-C. Jumas, C. A. Bridges, G. M. Veith, ""Characterization of sodium ion electrochemical reaction with tin anodes: Experiment and theory,"" *J. Power Sources* **2013**, *234*, 48–59.
[74] Z. Du, R. A. Dunlap, M. N. Obrovac, ""Investigation of the reversible sodiation of Sn foil by ex-situ X-ray diffractometry and Mössbauer effect spectroscopy,"" *J. Alloys Compd.* **2014**, *617*, 271–276.
[75] B. Zhang, G. Rousse, D. Foix, R. Dugas, D. A. D. Corte, J. Tarascon, ""Microsized Sn as Advanced Anodes in Glyme-Based Electrolyte for Na-Ion Batteries,"" *Adv. Mater.* **2016**, *28*, 9824–9830.